Single-lipid tracking on nanoscale membrane buds: The effects of curvature on lipid diffusion and sorting

Xinxin Woodward, Eric E. Stimpson, and Christopher V. Kelly[&]

Department of Physics and Astronomy, Wayne State University, Detroit, MI
[&] Corresponding author. Email: cvkelly@wayne.edu

KEYWORDS
Membrane curvature, single-particle tracking, molecular sorting, diffusion, lipid dynamics

ABSTRACT

Nanoscale membrane curvature in cells is critical for endocytosis/exocytosis and membrane trafficking. However, the biophysical ramifications of nanoscale membrane curvature on the behavior of lipids remain poorly understood. Here, we created a model system of curvature at physiologically-relevant scale have been created and obtained nanoscopic information on lipid distributions and dynamics. Supported lipid bilayers were created over 50 and 70 nm radius nanoparticles to create membrane buds and single-molecule localization microscopy was performed with diverse mixtures of fluorescent and non-fluorescent lipids. The use of Monte Carlo simulations to fit our results have yielded quantification of the effects of curvature on the lipid diffusion and sorting. Whereas the composition of the non-fluorescent lipids yielded minimal changes to the curvature effects, the labeling strategy of the fluorescent lipid yielded highly varying curvature effects. Most conditions yielded single-population Brownian diffusion throughout the membrane; however, curvature-induced lipid sorting, slowing and aggregation were observed. Head-group labeled lipids such as DPPE-Texas Red and POPE-Rhodamine diffused >2.4x slower on the curved vs. the planar bilayers; tail-labeled lipids such as NBD-PPC, TopFluor-PPC, TopFluor-PIP2, $DiIC_{12}$, and $DiIC_{18}$ displayed no significant changes in diffusion due to the membrane curvature.

1) INTRODUCTION

Nanoscale curvature of the plasma membrane is tightly regulated during endocytosis and exocytosis via the dynamics and sorting of membrane lipids and proteins [1–4]. For example, signaling lipids such as PIP_2 are concentrated at sites of endocytosis and exocytosis, although the mechanisms of its sorting are unknown [5,6]. Recent studies of lipid diffusion show a possible inherent sorting of lipids at curvature sites that correlate to the lipid molecular shape [7,8] and a significant slowing of single-lipid diffusion at correlated to membrane curvature [9]; however, both theoretical and experimental work often shows no lipid sorting correlated to lipid shape [10]. The underlying biophysical interplay between lipids and curvature are poorly understood despite numerous studies demonstrating the importance of lipid-composition-dependent bending rigidity, phase behavior, and molecular sorting [11].

The biophysics of lipids on membranes with nanoscale curvature has been studied with varying methods of creating curvature. Supported lipid bilayers (SLBs) on curved substrates have been studied on substrate engineered with photolithography [12], e-beam lithography [13], and nanoparticle (NP) deposition [7,14–16]. Liposomes of varying size have yielded relative protein and lipid partition coefficients [8]. And tethers pulled from giant unilamellar vesicles (GUVs) yield dynamically controlled radii in a cylindrical geometry [17–22]; however, sub-diffraction-limited resolution of lipid dynamics have been difficult to extract due to tubule dynamics. Only the technique of NP deposition enables the creation

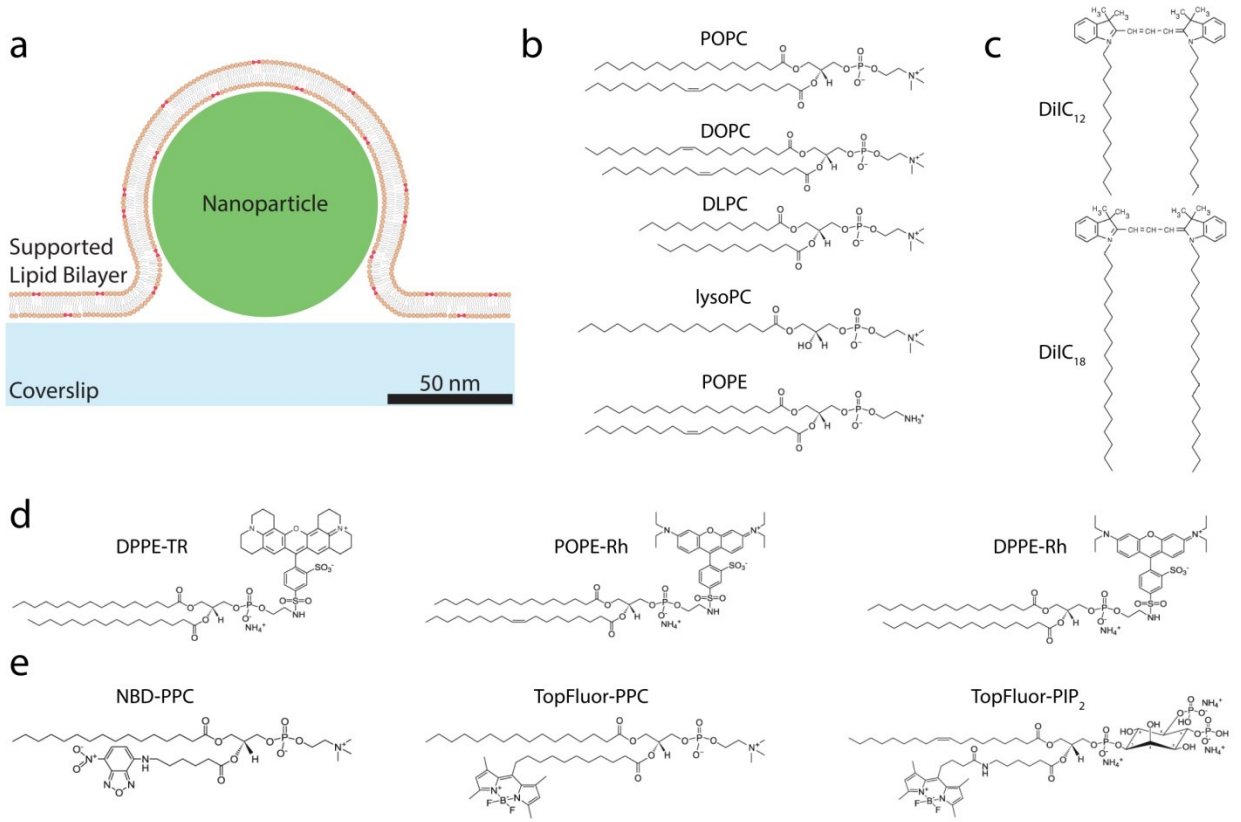

Figure 1: (a) Nanoscale membrane curvature was engineered by forming supported lipid bilayers over polystyrene nanoparticles on microscopy cover glass. Single-lipid localization and tracking were performed with varying membrane composition and fluorescent lipid. (b) Non-fluorescent membrane components. Fluorescent lipids tracked include (c) head-group labeled lipids, (d) lipidated carbocyanine dyes, and (e) tail-labeled lipids.

of nanoscale membrane curvature on the scale of natural endocytic/exocytic processes without the use of a cleanroom and with sufficient sample stability for super-resolution dynamics. With this NP-induced nanoscale membrane curvature, the sorting and dynamics of single proteins and lipids have been previously studied with varying the acyl tails of the fluorescent lipid [7], varying the radius of the NP [14], and to reveal cholera toxin subunit B sorting and diffusion at curvature sites [16].

A detailed understanding of the physical properties of lipids at sites of nanoscale curvature remains unknown. Theoretical estimates predict no significant sorting of lipids at curvature sites with radii of curvature > 50 nm [10]. However, greater curvature has been correlated with greater sorting of 5-hexadecanoylaminofluorescein [14], slowing of lipid diffusion [7,9], and curvature and composition coupling associates to lipid phase separation [18].

Within this manuscript, we report the effects of curvature on the diffusion and sorting of various fluorescent lipids in supported lipid bilayers of varying composition. Nanoscale curvature was created by bursting GUVs over polystyrene NPs of 50 and 70 nm radius. Super-resolution imaging and single particle tracking (SPT) were employed to measure the lipid diffusion coefficient and sorting. Results were compared to monte carol simulations that reproduce the effects of curvature in the experimental data to quantify the curvature effects in lipid diffusion and sorting. Additionally, the radial vs. azimuthal single-

lipid diffusion around the membrane bud and the accumulation of lipids at the curvature site revealed barrier-free diffusion of the lipids regardless of the membrane curvature. Changing the non-fluorescent membrane composition yielded comparatively small differences in the diffusion at curvature sites relative to flat bilayer; D_{flat}/D_{curved} = 3.2 to 4.9 for DPPE-TR for all non-fluorescent membrane compositions. Whereas there was a comparatively large variation in D_{flat}/D_{curved} for different fluorescent lipids; D_{flat}/D_{curved} = 0.9 to 2.8 for varying fluorescent lipids in a POPC bilayer. Although most lipids displayed Brownian diffusion on planar and curved membranes, DPPE-Rh formed immobile aggregates at the curvature sites. These results demonstrate the physical ramifications of nanoscale membrane curvature on single-lipid dynamics and sorting as well as the importance of the fluorophore labeling method.

2) MATERIALS AND METHODS

2.1) Sample dish preparation

SLBs were created on glass bottom dishes (MatTek Corp.). Dishes were rinsed with ethanol and dried under a nitrogen stream prior to a 10 sec cleaning with air plasma (Harrick Plasma). Polystyrene NPs were diluted in Milli-Q water then applied for 2 min, achieved a result of density less than 0.2 μm^{-2} for the curvature-inducing NPs and 0.01 μm^{-2} for the NPs used as fiducial markers. Two different single-colored fluorescent polystyrene NPs were used to create membrane curvature: 70 nm radius NPs with $\lambda_{ex} = 488$ nm (Fluoro-Max; Fisher Scientific), and 50 nm radius NPs with $\lambda_{ex} = 405$ nm (Fluoro-Max; Fisher Scientific) were used to engineering membrane curvature. Control experiments to verify minimal fluorescent bleed through between the NP and lipid channels have been demonstrated previously [15]. 50 nm radius, multi-colored fluorescent polystyrene NPs were used as fiducial markers to correct stage drift (TetraSpeck, ThermoFisher Scientific Technologies).

2.2) SLB formation and staining

SLBs were created by the fusion of GUVs. onto the glass coverslip and over NPs as performed previously [15,16]. Similar to as described in detail elsewhere [23], GUVs. were created by drying lipids in chloroform onto an electrically conducting indium tin oxide plate. A chamber was formed with custom trimmed silicone sheet and a second plate was fastened with binder clips. The chamber was filled with 200mM sucrose solution and subjected to an alternating voltage of 2 V_{rms} at 10 Hz for 3 hr, after which the chamber solution contained GUVs. of diameter from 1 µm to 50 µm. After the addition of 1 µL of 200 mM $CaCl_2$, GUVs. were applied to the coverslip for 15 minutes before being rinsed vigorously with 1x phosphate buffer saline (PBS; Sigma Aldrich) and 100 nM ethylenediaminetetraacetic acid (EDTA; Sigma Aldrich). This process yielded SLB patches with minimal defects over the NPs and coverslip.

SLBs were composed of non-fluorescent phospholipids and fluorescent lipids (Fig. 1). Five different non-fluorescent lipids were used: 1-palmitoyl-2-oleoyl-*sn*-glycero-3-phosphoch (POPC; Avanti Polar Lipids), 1,2-di-(9Z-octadecenoyl)-*sn*-glycero-3-phosphocholine (DOPC; Avanti Polar Lipids), 1,2-dilinoleoyl-*sn*-glycero-3-phosphocholine (DLPC; Avanti Polar Lipids), 1-palmitoyl-2-oleoyl-sn-glycero-3-phosphoethanolamine (POPE; Avanti Polar Lipids), and L-α-lysophosphatidylcholine (lysoPC; Avanti Polar Lipids). The inclusion of fluorescent lipids into the GUVs resulted in fluorescent lipids in both leaflets of the resulting SLB. When no fluorescent lipids were included in the GUVs, fluorescent lipids were later added to only the top leaflet of the SLBs via vector staining. Eight different fluorescent lipids were used: DPPE-TR (Life Technologies), TF-PPC (Avanti Polar Lipids), TF-PIP_2 (Avanti Polar Lipids), NBD-PPC (Avanti Polar Lipids), DPPE-Rh (Avanti Polar Lipids), POPE-Rh (Avanti Polar Lipids), 1,1'-Didodecyl-3,3,3',3'-

Tetramethylindocarbocyanine Perchlorate ($DiIC_{12}$, Life Technologies), and 1,1'-Dioctadecyl-3,3,3',3'-Tetramethylindocarbocyanine Perchlorate ($DiIC_{18}$, Life Technologies).

The vector staining solution was composed of 20 mol% fluorescent lipids and 80 mol% POPC. Creation of the vector staining solution included mixing the lipids in chloroform in a glass vial and drying for 1 hr. Lipids were mixed with ethanol to yield a stock of solution at 0.1 mM. 0.1 µL of lipids in ethanol was mixed with 1 mL PBS and 100 nM EDTA and vortexed for immediate addition to the previously non-fluorescent SLB. After 2 min, the sample was thoroughly rinsed with PBS. Vector-stained samples were imaged within 2 hours after staining so that most fluorescent lipids were in the top leaflet of the bilayer [24].

2.3) Imaging procedure

SLBs with engineered curvature were imaged on an inverted IX83 microscope with a 100x, 1.49 NA objective (Olympus), a 2x emission-path magnification (OptoSplit, Cairn Research), and an iXon 897-Ultra EMCCD camera (Andor Technologies). Continuous-wave diode lasers at 50-100 mW and wavelengths of 405, 488, 561, or 647 nm (Coherent Technologies) were used for fluorescence excitation. The imaging software SOLIS (Andor Technology) was used to acquire movies with a 128 pixels x 128 pixels region of interest at 537 Hz. Excitation was passed through a clean-up filter (zet405/488/561/647x, Chroma Corp.), reflected into the objective with a quad-band dichroic mirror (zt405/488/561/647rpc, Chroma Corp.) and the emission was isolated via an emission filters (BrightLine single-band filters, Semrock, Inc.) and a 4-band notch filter (zet405/488/561/640m, Chroma Corp.), as described previously [15].

Illumination of the indocarbocyanine dyes (*i.e.*, $DiIC_{12}$ and $DiIC_{18}$) was performed with p-polarized total internal reflection fluorescence (TIRF) microscopy, as is consistent with polarized localization microscopy [15]. This illumination method results in a greater probability of the fluorophores in the membrane perpendicular to the coverslip being excited and detected. All other fluorescent lipids were excited with a normally incident, linearly polarized excitation, consistent with an s-polarized TIRF excitation. Head-group labeled fluorescent lipids (e.g., Texas Red and Rhodamine) are expected to have negligible difference in their excitation probability dependent on the polarization of the incident light due to the flexible linker with which they are attached to the lipid and the random orientations they can take relative to the membrane. Tail-labeled fluorescent lipids (e.g., TopFluor and NBD) had a membrane orientation dependence in their localization probability with an increased probability of localization at the curvature site vs. on the planar SLB, similar to p-polarized excitation for DiI, as further discussed below.

2.4) Single-fluorophore localization

The Fiji plug-in ThunderSTORM [25,26] was used to calculate the locations of the optically isolated fluorescent lipids via fitting a 2D Gaussian to each image of each lipid. As reported by ThunderSTORM, localizations with intensity < 100 photons, Gaussian fit width < 15 nm, or location uncertainty > 45 nm were excluded from further analysis. Stage drift was corrected by removing the drift observed in the multicolored fiduciary NPs after a 300 frame smoothly. Differences between the observed center of membrane curvature and the NP were caused by chromatic aberrations. The center of the curvature in the lipid channel was estimated to be at the center of a 2D Gaussian fit to the lipid localizations close to as expected from observation of the NP directly.

2.5) Single-particle tracking

The trajectories of single fluorophores were identified by linking localizations from sequential frames by u-track [27] with a maximum search radius of 400 nm. The single-step lengths (v) were grouped by distance away from the NP center, and fit to a 2D Maxwell-Boltzmann distribution to find its diffusion coefficient D_{fit},

$$P(v) = \frac{v}{(2D_{fit}\Delta t)} e^{-\frac{v^2}{4D_{fit}\Delta t}}. \quad (1)$$

The corrected diffusion coefficient (D_{xy}) was found from D_{fit} by considering the systematic error caused by image blur and localization uncertainty [9]. The time between sequential frames (Δt = 1.86 ms), the single-frame camera exposure time (t_{exp} = 1.70 ms), and the single-fluorophore localization uncertainty (σ_r = 17 to 35 nm) contribute to this calculation according to

$$D_{xy} = \frac{D_{fit} - \frac{\sigma_r^2}{2\Delta t}}{1 - \frac{t_{exp}}{3\Delta t}} \quad (2)$$

The lipid diffusion coefficient is reported as D_{xy} to be explicit that the observation methods employed here only reveal the diffusion through the *xy* imaging plane. When the membrane was not parallel to the coverslip, the embedded lipids diffused in the z-direction, which was not directly tracked here. The effects of membrane topography on D_{xy} are shown in the Monte Carlo simulations throughout this manuscript to distinguish between z-motion of the lipid and changes to the local lipid mobility within the bilayer.

The radial and azimuthal diffusion of the lipids relative to the NP-created membrane curvature were analyzed, as described in greater detail in the Supplemental Material (Eq. S1). Briefly, the square of the radial component of the step lengths was proportional to the radial diffusion coefficient (D_r). The square of the step lengths perpendicular to radial component was proportional to the azimuthal diffusion coefficient (D_θ). A Brownian diffuser on a flat bilayer would show $D = D_r = D_\theta$. The ratio of D_r/D_θ contains information on the inherent effects from the 2D projection of the curved membrane, non-Brownian behavior to diffusion, and variable observation probabilities with membrane curvature.

2.6) Monte Carlo simulation methods

Monte Carlo simulations were performed to understand the effects of varying parameters in a minimalistic physical model of membrane curvature. The simulations were varied to reveal the model parameters that best mimicked experimental results. The membrane shape was approximated as a conformal coat around the NP until a minimum of a 20 nm radius of curvature membrane neck connected the membrane smoothly to the surrounding planar supported lipid bilayer (Fig. 1A).

Single-lipid trajectories were mimicked by pseudo-randomly stepping across the membrane topography on a pre-defined set of possible lipid locations that were placed at a density of 4 per nm^2. Each step consisted of the lipid moving to one of the 110 ± 10 points within 3 nm on the simulated membrane with an average step distance of 2 nm, as done previously [9]. The time corresponding to each simulation step was set to fit a given diffusion coefficient on a planar membrane. For example, the time between each step corresponding to 0.45 μs replicates D = 2.5 μm^2/s on a planar membrane. The magnitude of curvature-induced changes to lipid diffusion was simulated by mimicking a different local D on all membrane area above the SLB, which manifested in the simulations as an altered time between steps. Locations separated by 1.86 ms from the simulated trajectories were recorded, a 20 nm standard

deviation Gaussian localization imprecision was applied, and the step lengths across the sample were analyzed just as was done for the experimental data with $t_{exp} = 0$. This model treated all curved membrane the same and yielded a ratio of D_{flat}/D_{curved} with which to compare systems (Figs. 2-4). Additionally, the ratio of radial to azimuthal diffusion was analyzed from the simulations (Fig. 5).

Simulations were used to mimic curvature-induced sorting of the lipids beyond that which would be expected solely from the increased membrane area. The fluorescent lipids per area on the curvature (ρ_{curved}) vs. the fluorescent lipids per area on the planar SLB (ρ_{flat}) was fit to match the radial density of lipid locations experimental data (Fig. 6). For example, a doubling of the fluorescent lipid concentration with curvature was simulated double the fluorescent lipid density for all membrane above the SLB vs. the lipid density on the SLB, which we report as $\rho_{curved}/\rho_{flat} = 2$.

The lines plotted throughout this manuscript represent the simulated results with parameters fit to the experimental results, which are plotted as symbols (Figs. 2-6). The best-fit parameters are shown in Tables 1-3, as determined by a X^2 minimization [15,28].

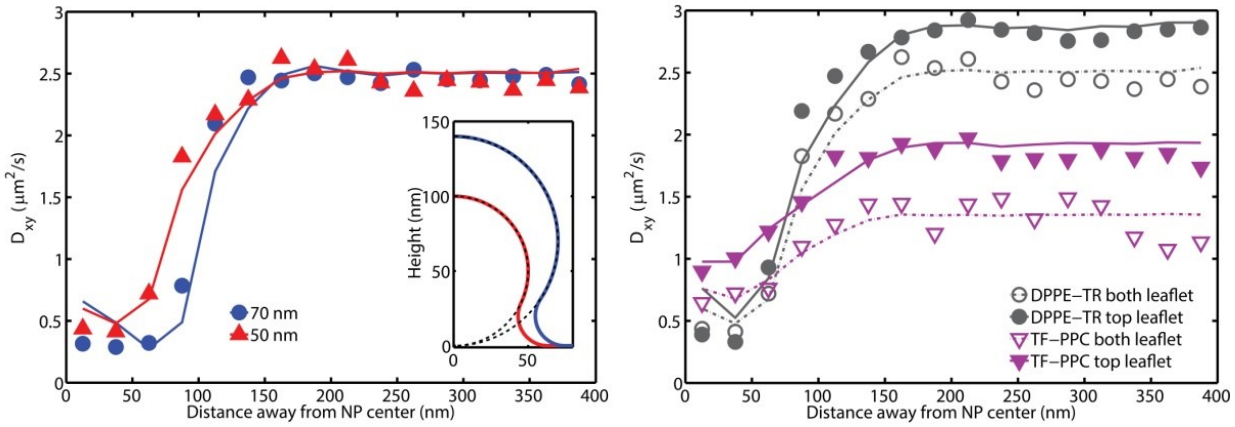

Figure 2: Diffusion through the xy-plane was measured for (A) DPPE-Rh on nanoparticles of 50 nm and 70 nm radius. (B) The observed diffusion varied with the fluorophore type and the labeling method. Fluorophores were either mixed into both bilayer leaflets during the GUV formation or added to top leaflet after SLB formation. Solid lines are fits from the Monte Carlo simulations (Table 1).

Table 1: Comparison of staining method and nanoparticle sizes.

System Number	Fluorophore	Staining method	NP size (nm)	D_{flat} (μm²/s)	D_{flat}/D_{curved}	$\rho_{curved}/\rho_{flat}$
1	DPPE-TR	both	70	2.5 ± 0.2	3.9 ± 0.2	2.1 ± 0.1
2	DPPE-TR	top	50	2.8 ± 0.1	2.4 ± 0.3	1.4 ± 0.1
3	DPPE-TR	both	50	2.4 ± 0.1	2.5 ± 0.1	2.9 ± 0.1
4	TF-PPC	top	50	1.8 ± 0.1	1.0 ± 0.1	2.5 ± 0.1
5	TF-PPC	both	50	1.3 ± 0.1	1.0 ± 0.1	6.7 ± 0.5

3) RESULTS

3.1) NP size and membrane-substrate interactions

The trajectories of single lipids were tracked within SLBs with engineered curvature. The SLBs were created through the bursting of GUVs over polystyrene NPs of varying diameter (Figs. 2A). The 3D

single-lipid trajectories were projected onto the xy imaging plane without preserving information on the fluorophore motion in the z-direction. The experimentally measured diffusion coefficient (D_{xy}) depends on the local orientation of the membrane, the local diffusion coefficient within the membrane, and the acquisition frame rate by averaging across the sample [9]. Membranes with their normal vectors parallel to the z-axis have faster D_{xy} than membranes with normal vectors angled away from the z-axis. The curvature effects on lipid diffusion correlated with the NP size; NPs of radii 50 and 70 nm demonstrated curvature-influenced diffusion out to radii of 78 ± 19 and 99 ± 16 nm, respectively (Fig. 2A).

The membrane-substrate interaction slows the diffusion of molecules within the bilayer. The polystyrene NPs and the glass coverslip supporting the bilayer interacted with the bilayer and affected the two bilayer leaflets differently. The single-lipid diffusion was compared in samples that had the fluorescent lipids in both bilayer leaflets and samples that had the fluorescent lipids in only the top leaflet (Fig. 2B). The effects of the membrane-substrate interaction on the single-lipid diffusion on the top leaflet are expected to be minimal. We observed the diffusion of top-leaflet only labeling to be 1.2 ± 0.1 and 1.4 ± 0.2 times faster than both-leaflet labeling for DPPE-TR and TF-PPC, respectively, consistent with prior observations [29]. For both DPPE-TR and TF-PPC, we observed similar effects of the membrane curvature regardless of the labeling method, suggesting that the curvature-affected diffusion was not due solely to the variations in membrane-substrate interaction on the NP vs. coverslip. Differences between top-only and both leaflet labeling at the curvature may additionally be caused by the difference in the sign of the curvature in the top and bottom leaflet, but this difference was not distinguishable from the substrate effects in the experimental results.

In considering only the lipid trajectories on the flat glass coverslip (i.e., >250 nm from the NP), the differences between the lipid diffusion on the top vs. bottom leaflets were estimated. DPPE-TR displayed a 17% faster diffusion in the top leaflet vs. both leaflets with D = 2.9 and 2.4 $\mu m^2/s$, respectively. Assuming an equal population of diffusers in both leaflets, D for bottom-only DPPE-TR is estimated to be 1.9 $\mu m^2/s$. TF-PPC displayed a 38% faster diffusion in the top leaflet vs. both leaflets with D of 1.8 and 1.3 $\mu m^2/s$, respectively. Assuming an equal population of diffusers in both leaflets, D for bottom-only TF-PPC is estimated to be 0.8 $\mu m^2/s$.

3.2) Matching experimental and Monte Carlo results

Efforts to mimic the observed D_{xy} vs. distance from the NP with minimalistic Monte Carlo simulations revealed that for some system compositions, the lipid diffusion was slower at the site of membrane curvature than would be expected if the lipids diffused at a rate independent of membrane curvature. A simplistic assumption that all curved-membrane yields consistently altered lipid diffusion enabled fitting the Monte Carlo predictions to the experimental results with the ratio of the diffusion rate on flat membrane compared to that of the curved membrane (D_{flat}/D_{curved}). The experimentally measured D_{xy} of TF-PPC did not require D_{flat}/D_{curved} to vary significantly from unity but fitting the Monte Carlo simulations to the DPPE-TR experimental data required $D_{flat}/D_{curved} \geq 2.4$ (Tables 1-3). D_{flat}/D_{curved} did not significantly depend on the overall composition of the membrane (Fig. 3, Table 2) but it did depend on fluorescent lipid type (Fig. 4, Table 3).

3.3) Varying the membrane composition

Six different phospholipid bilayer compositions were used to reveal the effects of non-fluorescent lipids and curvature in lipid diffusion. DPPE-TR lipids were tracked in both bilayer leaflets with curvature created over 70 nm radius NPs (Fig. 3, Table 2). Membrane consistently included 0.05 mol% DPPE-TR. The

inclusion of lysoPC and POPE tested the effects of adding lipids of varying shape; lysoPC has large head-group compared to its tails and the DPPE as a small head-group relative to its tails. By comparing POPC, DOPC, and DLPC, the impact of acyl tail length and saturation were examined while maintaining a liquid disordered phase. POPC, DOPC, and DLPC have varying degrees of acyl tail order and phase transition temperatures of -2°C, -17°C, and -57°C, respectively. Changing the membrane composition surrounding the DPPE-TR had minimal effects on D_{flat}/D_{curved} and D_{flat}.

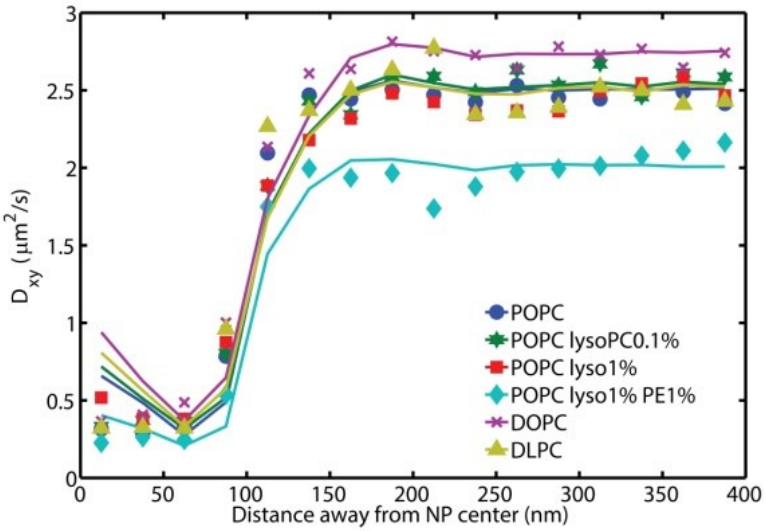

Figure 3: Varying the non-fluorescent membrane composition had a minimal effect on the observed diffusion of DPPE-TR. Curvature was created by a 70 nm NP and DPPE-TR was included in both leaflets. Solid lines are fits from the Monte Carlo simulations (Table 2).

Table 2: Comparison of membrane composition.

System Number	Fluorophore	Membrane composition	NP size (nm)	D_{flat} ($\mu m^2/s$)	D_{flat}/D_{curved}	$\rho_{curved}/\rho_{flat}$
1	DPPE-TR	POPC	70	2.5 ± 0.2	3.9 ± 0.2	2.1 ± 0.1
2	DPPE-TR	DOPC	70	2.8 ± 0.2	2.9 ± 0.2	1.5 ± 0.1
3	DPPE-TR	DLPC	70	2.5 ± 0.2	3.2 ± 0.3	1.3 ± 0.1
4	DPPE-TR	POPC lysoPC0.1%	70	2.6 ± 0.2	3.5 ± 0.1	2.2 ± 0.1
5	DPPE-TR	POPC lysoPC1%	70	2.5 ± 0.2	3.2 ± 0.3	2.8 ± 0.1
6	DPPE-TR	POPC lysoPC1% PE1%	70	2.1 ± 0.2	4.9 ± 0.2	2.5 ± 0.1

3.4) Varying the molecular structure of the fluorescent lipid

Eight different fluorescently labeled lipids were tracked in the top leaflet of a POPC bilayer and over a 50 nm radius NPs (Fig. 4). The single-lipid diffusion varied between fluorescent lipid types. The three headgroup-labeled phospholipids were POPE-TR, POPE-Rh, and DPPE-Rh; they displayed the fastest planar membrane diffusion and the most change with membrane curvature compared to the other types of fluorescent lipids. Fluorescent lipophilic cationic indocarbocyanine dyes with either 12 or 18 carbons per tail (i.e., $DiIC_{12}$ and $DiIC_{18}$) displayed the slowest diffusion in the bilayer of the fluorophores tested.

The three tail-labeled phospholipids were NBD-PPC, TF-PIP2, and TF-PPC; they displayed the least effects of curvature of all tested fluorophores. The tail-labeled lipids and DiI each displayed D_{flat}/D_{curved} indistinguishable from unity.

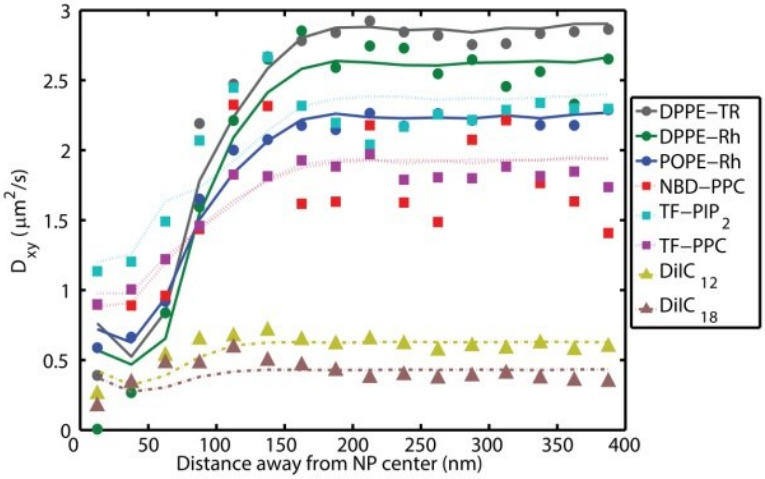

Figure 4: Varying the fluorescent lipid tracked had large effects on the observed diffusion. Curvature was created by a 50 nm NP and fluorescent lipids were included in only the top leaflets. Solid lines are fits from the Monte Carlo simulations (Table 3).

Table 3: Comparison of fluorescent lipids.

System Number	Fluorophore	Membrane composition	NP size (nm)	D_{flat} (μm²/s)	D_{flat}/D_{curved}	$\rho_{curved}/\rho_{flat}$
7	DPPE-TR	POPC	50	2.8 ± 0.1	2.4 ± 0.3	1.4 ± 0.1
8	DPPE-Rh	POPC	50	2.5 ± 0.1	2.8 ± 0.3#	8.2 ± 0.4#
9	POPE-Rh	POPC	50	2.2 ± 0.1	1.6 ± 0.1	1.6 ± 0.1
10	TF-PPC	POPC	50	1.8 ± 0.1	1.0 ± 0.1	2.5 ± 0.1*
11	TF-PIP_2	POPC	50	2.3 ± 0.2	0.9 ± 0.1	2.5 ± 0.1*
12	NBD-PPC	POPC	50	1.8 ± 0.5	1.1 ± 0.6	15.0 ± 0.3*
13	$DiIC_{12}$	POPC	50	0.59 ± 0.03&	1.1 ± 0.1&	7.5 ± 0.1*
14	$DiIC_{18}$	POPC	50	0.37 ± 0.02&	0.9 ± 0.1&	7.0 ± 0.3*

Comparison of these numbers may be limited because of (#) non-Brownian diffusion at curvature sites, (*) localization probabilities that varied with membrane orientation, and (&) two populations of diffusers.

Most fluorescent lipids displayed Brownian diffusion across the sample with no significant aggregation and only one population of diffusers. Exceptions include $DiIC_{12}$ and $DiIC_{18}$ that displayed two populations of diffusers in the planar bilayers and DPPE-Rh which underwent curvature-induced aggregation and apparent immobility in the curved bilayer. The two populations within the $DiIC_{12}$ and $DiIC_{18}$ samples were found through analysis of the histogram of step lengths (Fig. S1). On flat bilayers, the histograms did not fit well to the expected 2D Maxwell-Boltzmann distribution for a single population of identical diffusers (Eq. 1) but it did fit well to the expected distribution of two populations of diffusers with different diffusion coefficients (Eq. S2). When fitting to two populations of diffusers, $DiIC_{12}$ and $DiIC_{18}$ both yielded 65 ± 5 % of the diffusers in the faster diffusing population, and rest of the diffusers in the slower diffusing population. By comparison, similarly fitting the other fluorescent lipids to two populations of diffusers consistently yielded <6% of the diffusers in the second population. When the membrane was

curved around the NP, the curvature-induced slowing resulted in the histograms of step lengths for $DiIC_{12}$ and $DiIC_{18}$ became insignificantly different than expected for single-population Brownian diffusion, although the resolution of two populations was limited by due to the single-fluorophore localization uncertainty and slower diffusion coefficient. For a direct comparison between systems, the results shown in the body of this manuscript analyze the $DiIC_{12}$ and $DiIC_{18}$ diffusion as a single population and the two-population analysis is shown in the Supplemental Material.

3.5) Radial vs. azimuthal diffusion

The single-particle tracking trajectories were analyzed to reveal the diffusion rates radially and azimuthally on to the membrane bud. The ratio of the diffusion radial to the bud (D_r) to the diffusion azimuthally around the bud (D_θ) quantifies the preference for the lipids to move towards and away from the bud vs. around the bud. Monte Carlo simulations estimated how locally Brownian diffusion would appear with a 2D projection from the 3D membrane topology. The diffusion of DPPE-TR in the varying membrane compositions yielded D_r/D_θ ratios that were indistinguishable from locally Brownian diffusion on the membrane bud (Fig. 5). Accordingly, there was no apparent barrier to diffusion or increased probability of the lipids to diffuse around rather than up-and-down the membrane bud.

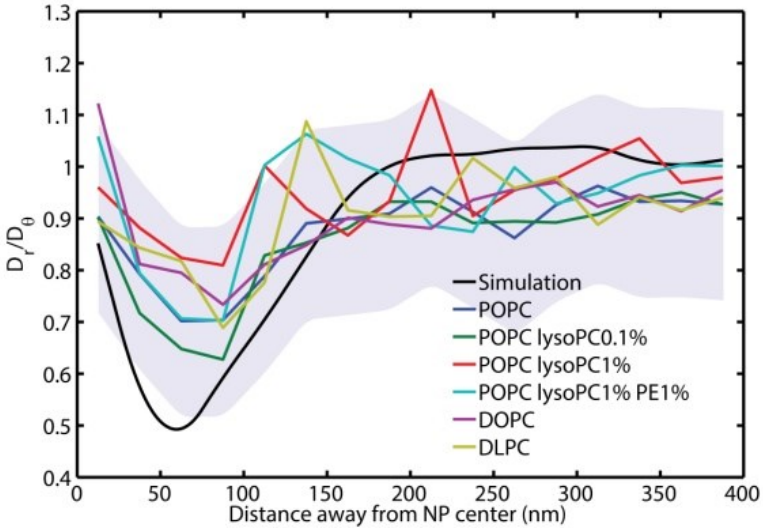

Figure 5: The ratio of the radial vs. azimuthal diffusion is not significantly different than that of Brownian diffusion on the engineered membrane curvature. DPPE-TR was tracked in both bilayer leaflets over 70 nm NPs. The shaded purple region represents the range of confidence for the diffusion with DOPC.

3.6) Lipid density vs. distance from NP

The super-resolution images of lipid localizations relative to membrane curvature were analyzed to reveal the probability of a fluorescent lipid being localized at the site of curvature vs. on the surrounding planar SLB. The azimuthal average of the localizations yielded the number lipids localized vs. distance from the NP (Fig. 6). Monte Carlo simulations provided a quantification of these results by comparing the increased concentration per membrane area of localizations on the curved membrane vs. the planar membrane (*i.e.*, $\rho_{curved}/\rho_{flat}$). The head-group labeled lipids consistently yielded $\rho_{curved}/\rho_{flat} > 1$, as expected for $D_{flat}/D_{curved} > 1$.

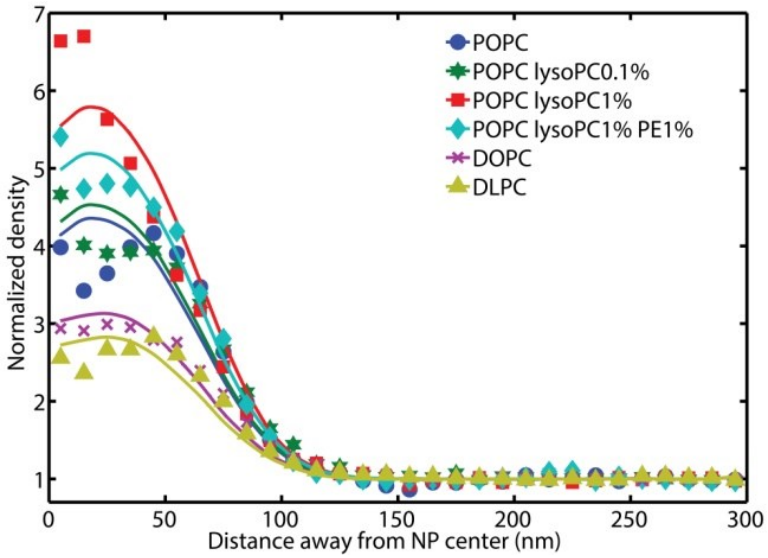

Figure 6: The radial density of fluorescent lipids localizations reveals sorting of the fluorescent lipid to the nanoparticle-created curvature. Solid lines are fits from the Monte Carlo simulations (Table 2).

4) DISCUSSION

Membrane curvature may significantly affect the diffusion and sorting of individual lipids; however, many parameters affect the magnitude of this effect, including membrane curvature radius, lipid acyl tails, temperature, membrane tension, and membrane composition [8,17–22,30–32]. Here we show how membrane composition and fluorescent labeling methods affect the dependence of single-lipid diffusion relative to membrane curvature. For example, DPPE-TR and TF-PPC had D_{flat}/D_{curved} = 2.5 ± 0.2 and 1.0 ± 0.1, respectively (Figs. 2, 4) while varying the surrounding lipid composition had minimal effect on the D_{flat}/D_{curved} of DPPE-TR (Fig. 3).

Within the diverse experimental systems used to reveal the effects of membrane curvature, the interplay between the interdependent membrane properties can be difficult to disentangle. For example, membrane tubules created from GUVs necessitate an externally applied membrane tension [22,33] and the partition coefficient on to LUVs are typically studied at saturating concentrations of the fluorescent lipid [8]. The membrane curvature engineered into SLBs, as done here, allows for coupling between planar and curved membranes with variable fluorophore concentrations, but poorly controls the membrane tension and introduces membrane-substrate interaction effects. SLB patches created by GUV fusion have shown variation in membrane tension across the sample [16]. The NP-created membrane engineering performed here provides membrane bud topographies that are of the physiologically relevant length scales without the use of a cleanroom and with sufficient sample stability to perform super-resolution optical techniques.

4.1) Fluorophore charge and residency

The fluorescent lipid labeling strategy had significant effects on its diffusion. Broadly, we observed that the head-group labeled lipids diffused fastest on the planar membrane and experienced the most slowing at curvature sites. The tail-labeled lipids diffused slightly slower on planar membranes but had no observable changes in their diffusion rates at curvature sites. And DiI demonstrated two populations of diffusers, both of which were the slowest on planar membranes and were not affected by membrane

curvature. Insights into the mechanisms behind these observations are gained by comparison to prior molecular dynamics simulations.

Although commonly discussed, there is increasing consensus that a naive molecular shape description is insufficient to predict the curvature-induced sorting of individual lipids [10]. While it is tempting to model lysoPC as a cone-shape with a large headgroup that would sort to positive curvature and POPE as a cone-shape with a small head-group that would sort to negative curvature within a cylindrical POPC bilayer, we see no significant differences in single-lipid trajectories when incorporating lysoPC or POPE at <1 mol% to our samples (Fig. 3). Further, there is qualitatively no difference in the effects of curvature between incorporation of fluorescent lipids into only the top, positively curved leaflet or both leaflets (Fig. 2). Prior studies have explained lipid sorting with curvature-dependent densities of defect sites and a molecular shape-dependent binding affinity to the defects [7,8].

Varying the charge of fluorescent lipids can have dramatic effects on its lateral diffusion with the membrane. For example, all-atom simulations of 1,6-diphenylhexatriene (DPH) and its trimethylammonium derivative (TMA-DPH) in DPPC bilayer revealed a 3x difference in its lateral diffusion coefficient in a DPPC bilayer [34]. The charged TMA-DPH diffused indistinguishably from the DPPC with and without cholesterol and with and without counter ions; however, the uncharged DPH fluorophore consistently diffused faster than DPPC. This difference was attributed to the varying electrostatic interactions between the fluorophores and the phospholipids and was not the cause of varying fluorophore probe localization within the bilayer, molecular volumes, or probe-induced variations to the lateral pressure profile [34]. Similarly, TR-DPPE was observed to form electrostatic interactions with DPPC via all-atom molecular dynamics simulations with each Texas Red bound to 1.2 DPPC molecules and the DPPC molecules diffusing 1.5x faster than TR-DPPE [35].

Molecular dynamics simulations have additionally provided insights into the localization of the fluorophores within the bilayer. Texas Red was found to reside in the upper acyl chain region of the bilayer, below that which would be expected if the fluorophore was assumed to be an extension of the head group [36] and experimental results have shown similar penetration into the membrane for Texas Red and Rhodamine [37]. These results show the difficulty in predicting the location of the fluorophore within the membrane even in flat membranes.

In curved membranes, the spacing between lipid head-groups and water penetration into the leaflet both increase for positive curvature and both decrease for negative curvature. Accordingly, one would expect penetration of fluorophores into the leaflet deeper for positive curvature and shallower for negative curvature. It is therefore surprising that our results show a consistent effect of curvature when the fluorescent lipids are confined to the top, positively curved leaflet or incorporated into both leaflets. The mechanism of curvature-affected diffusion may be different in the two curvatures. We hypothesize that positive curvature enables greater electrostatic interactions between the head-group labeled lipids and the surrounding phospholipids while negative curvature encourages greater membranes-substrate interaction. However, these hypotheses are highly speculative and worthy of further examination.

4.2) Substrate-membrane interactions

The effects on the substrate on the supported bilayer vary with the substrate roughness, surface chemistry, and the membrane properties to be observed [38,39]. The substrate effects are smaller for single-lipid diffusion as compared to the diffusion of transmembrane protein or membrane domain (*i.e.,* lipid raft). However, the 1.17 and 1.38x increase in planar bilayer diffusion in top-leaflet and bottom-leaflet D on planar bilayers for DPPE-TR and TF-PPC, respectively, is consistent with the 1 to 2.5x

differences seen previously for SLBs glass [40–42][42](42)(43). We speculate that the SLB formation method employed here via GUV fusion incorporates less tension into the SLB than SLBs formed via SUV fusion and this decreased tension may also decrease the effects of the substrate on the membrane dynamics.

4.3) Localization probabilities of rotationally-confined fluorophores

The localization probability of a single fluorophore depends on the overlap between the excitation light and the transition dipole moment of the fluorophore. This is a key principle behind polarized localization microscopy for the detection of nanoscale membrane budding events with fluorophores that maintain a regular orientation relative to their local membrane orientation (*i.e.*, DiI, Bodipy, or NBD) [15]. Many hydrophilic fluorophores that are attached via a flexible linker (*i.e.*, head-group labeled Rhodamine and Texas Red) effectively tumble within the sample sufficiently to remove any significant dependence on the localization probability to the excitation light polarization or the membrane orientation. Fluorescent lipids such as DiI and tail-labeled NBD, however, can display emission intensities that vary by up to 3-fold dependent on membrane orientation, which can yield apparent higher densities of localizations at the curvature site and a bias in the single-particle tracking results [15,43–45]. As such, the distributions of localizations for rotationally confined fluorophores do not directly reflect their concentration in the membrane.

The localization density and D_r/D_θ analyses for tail-labeled lipids and DiI incorporated both variations in the local concentration of the fluorophores and a localization probability that was dependent on the light polarization and membrane orientation. Because of these intertwined variables, the density of localizations and D_r/D_θ for these lipids were not analyzed in this manuscript.

Monte Carlo simulations were performed to estimate the effects of varying localization probabilities on the diffusion and density results (Fig. S2), as explained more fully in the Supplemental Material. In brief, both the diffusion and density analyses provide a greater sampling of the membrane vertical to the coverslip when p-polarized excitation light is used for DiI and s-polarized light is used for NBD or TopFlour. This resulted in our inability to distinguish between variations in the observed localization density being caused by changes to the single-lipid sorting or the varying localization probability (Fig. S2D). However, varying localization probabilities reveals a characteristically different effect than varying D_{flat}/D_{curved} (Fig. S2E) and the effects of curvature on the diffusion of all fluorophores has been analyzed (Fig. 4).

4.4) Connecting diffusion rates and binding site densities

Prior understandings of the curvature-dependent sorting and diffusion rates of individual lipids have considered an effective binding site density that was dependent on membrane curvature [7,8,14,46]. The relationship between defect density and curvature likely varies between vesicles and SLBs. Small vesicles are highly curved, high-energy structures with slow flip-flop such that the outer and inner leaflets may have highly varying lateral pressure profiles. SLBs patches as studied here do not require lipid flip-flop to relive different leaflet tension since lipids may diffuse between leaflets around the edge of the patch.

The density of defects and the energetics of diffusing between defects could affect the diffusion rate (D) of a single lipid. If the fluorescent lipid binding sites were on a locally planar square lattice, D would depend linearly on the stepping frequency (ν) and quadratically on the lattice spacing (Λ) according to $D = 0.25\nu\Lambda^2$. Consequently, the binding site density is inversely proportional to the D and $\rho \propto \Lambda^{-2}$. If ν is

constant, then $D_{flat}/D_{curved} = \rho_{curved}/\rho_{flat}$; deviations from this equality could be represented by varying v. The activation barrier for single steps on the curved (E_{curved}) and flat (E_{flat}) membrane could depend on binding site density and give an exponential effect on v such that

$$\frac{D_{flat}}{D_{curved}} = \frac{\rho_{curved}}{\rho_{flat}} e^{(E_{curved}-E_{flat})/(k_B T)}, \quad (3)$$

with the Boltzmann constant (k_B) and temperature (T). Through fitting a straight line through all experimental data for head-group labeled lipids in both leaflets over 70 nm radius NPs (Fig. S3), it was calculated that $\langle E_{curved}\text{-}E_{flat}\rangle = 0.5\ k_B T$. This implies that although the binding sites are denser on the curved vs. planar membrane, there is a greater energy barrier to step between them.

4.5) Non-Brownian Diffusion

All the fluorescent lipids studied here except $DiIC_{12}$ and $DiIC_{18}$ had single-population Brownian diffusion on the planar membrane; $DiIC_{12}$ and $DiIC_{18}$ demonstrated two distinct populations of diffusion coefficients on the planar membrane. This could be due to a chemical degradation of our fluorescent lipid stock or a naturally occurring distribution in aggregation state of the fluorescent lipids. Similar complexities to DiI diffusion have been previously observed [47]. No curvature-induced lipid slowing was observed via either analysis method or DiI acyl tail length (*i.e.,* $D_{flat}/D_{curved} = 1.0 \pm 0.1$). Assuming the $D_{flat}/D_{curved} = \rho_{curved}/\rho_{flat}$, as described above, the lack of affect curvature has on DiI diffusion is consistent with the lack of affect curvature has on DiI sorting [8,21]. These results show less effect of curvature on DiI diffusion and sorting than our prior measurements [15], which we speculate were caused by the differences in the sample buffers, imaging conditions, and/or lipid oxidation and are under further investigation.

At the curvature sites, DPPE-Rh demonstrated non-Brownian diffusion at the sites of nanoscale membrane curvature. The two main indicators of the non-Brownian diffusion are the exceptionally small values of D_{xy} ($r < 25$ nm) and the shape of the radial histogram of DPPE-Rh localizations, which were consistent with the DPPE-Rh at each curvature site accumulating into an immobile cluster. The single-lipid diffusion was consistent with immobile lipids and the radial distribution of localizations was not wider than would be expected from the single-fluorophore localization uncertainty of a small stationary accumulation of fluorophores. This fundamentally different diffusive behavior for DPPE-Rh may be attributable to the high propensity of this fluorophore to cause peroxide formation, lipid oxidization, and membrane domain formation upon exposure to light; DPPE-Rh has been experimentally shown to cause more light-induced membrane degradation than DPPE-TR, NBD-PPC, or $DiIC_{18}$ [48]. Although the fluorophore concentration is very low in these experiments (0.05 mol%), the fluorescence illumination was intense at >15 kW/cm^2 for >10 min.

4.6) Monte Carlo model simplifications

The two primary phenomena not represented in our Monte Carlo simulations are the variations between leaflets and the effects of varying curvature at the bud. The two bilayer leaflets have curvature of opposite sign and differing interaction with the substrate that were not modeled. Additionally, the membrane bud is attached to the surrounding planar SLB via a membrane neck with a negative Gaussian curvature. The effects of curvature on lipid dynamics and sorting would presumably change with both the sign of the principal curvature and the magnitude of the Gaussian curvature. The incorporation of these variables into the Monte Carlo simulations performed here would have yielded excessive, inter-

dependent fitting variables. The accuracy of the Monte Carlo modeled here is adequate to mimic the average effect of membrane curvature on lipid behavior by only fitting to D_{flat}, $D_{curved,}$ and $\rho_{curved}/\rho_{flat}$.

5) CONCLUSIONS

Nanoscale membrane curvature was engineered by draping SLBs over NPs on a microscope coverslip. The diffusion and sorting of eight different fluorescent lipids were observed in six different non-fluorescent lipid compositions. Single-molecule localization data were analyzed to yield the lipid diffusion and sorting relative to the membrane curvature. Experimental data were fit to Monte Carlo simulations to quantify the effective slowing and sorting of the lipids. The fluorescence labeling strategy affected the curvature-dependence on lipid diffusion more than varying the composition of the non-fluorescent surrounding lipids. The head-group labeled lipids showed slowing and accumulation at curvature sites. Tail-labeled lipids and DiI show no significant slowing at curvature sites. The distribution of step lengths is consistent with a single-population Brownian diffusion for DPPE-TR, POPE-Rh, NDB-PPC, TF-PPC, and TF-PIP2 on planar and curved membranes. This was further supported matching experiments and simulations of D_r/D_θ for DPPE-TR over the membrane bud. However, $DiIC_{12}$ and $DiIC_{18}$ displayed two populations of diffusers and DPPE-Rh displayed curvature-induced immobilization and aggregation. These results show the capability of nanoscale membrane curvature to affect lipid behavior with a strong dependence on fluorophore labeling.

6) ACKNOWLEDGEMENTS

The authors thank Jeffery Potoff, Umit Ozer, Abir Kabbani, Timothy Susman, Logan Nguyen, Eric Stimpson, William Wickens for valuable discussions. Monte Carlo simulations were performed on the Wayne State University High Performance Computing Grid. Financial support was provided by Wayne State University laboratory startup funds and Richard J. Barber. This material is based upon work supported by the National Science Foundation under Grant No. DMR1652316.

7) ABBREVIATIONS

D, diffusion coefficient;
D_θ, azimuthal diffusion coefficient;
D_r, radial diffusion coefficient;
D_{flat}, diffusion coefficient at flat bilayer;
D_{curved}, diffusion coefficient on curved bilayer;
$DiIC_{12}$, 1,1'-Didodecyl-3,3,3',3'-Tetramethylindocarbocyanine Perchlorate;
$DiIC_{18}$, 1,1'-Dioctadecyl-3,3,3',3'-Tetramethylindocarbocyanine Perchlorate;
DLPC, dilinoleoyl-glycero-3-phosphocholine;
DOPC, dioleoyl-glycero-3-phosphocholine;
DPPC, dipalmitoyl-glycero-phosphocholine;
DPPE-Rh, dipalmitoyl-glycero-3-phosphoethanolamine-N-(lissamine rhodamine B sulfonyl);
DPPE-TR, Dihexadecanoyl-Glycero-3-Phosphoethanolamine;
GUV, giant unilamellar vesicle;
Λ, step distance;
lysoPC, 1-palmitoyl-2-hydroxy-sn-glycero-3-phosphocholine;
MSR, max searching radius;
MSD, mean square displacement;

NBD-PPC, 1-palmitoyl-2-{6-[(7-nitro-2-1,3-benzoxadiazol-4-yl)amino]hexanoyl}-sn-glycero-3-phosphocholine;
v, step frequency;
NP, nanoparticle;
PLM, polarized localization microscopy;
POPC, palmitoyl-oleoyl-glycero-phosphocholine;
POPE, 1-palmitoyl-2-oleoyl-sn-glycero-3-phosphoethanolamine;
POPE-Rh, 1,2-dioleoyl-sn-glycero-3-phosphoethanolamine-N-(lissamine rhodamine B sulfonyl);
r, distance away from NP center;
ρ, density of fluorophores;
SLB, supported lipid bilayer;
SPT, single particle tracking;
TF-PPC, 1-palmitoyl-2-(dipyrromethene boron difluoride)undecanoyl-sn-glycero-3-phosphocholine;
TF-PIP_2, 1-oleoyl-2-{6-[4-(dipyrromethene boron difluoride)butanoyl]amino}hexanoyl-sn-glycero-3-phosphoinositol-4,5-bisphosphate;

8) REFERENCES

[1] C.V. Kelly, M.G. Liroff, L.D. Triplett, P.R. Leroueil, D.G. Mullen, J.M. Wallace, S. Meshinchi, J.R. Baker, B.G. Orr, M.M. Banaszak Holl, Stoichiometry and Structure of Poly(amidoamine) Dendrimer−Lipid Complexes, ACS Nano. 3 (2009) 1886–1896. doi:10.1021/nn900173e.

[2] M.M. Kozlov, H.T. McMahon, L.V. Chernomordik, Protein-driven membrane stresses in fusion and fission, Trends Biochem. Sci. 35 (2010) 699–706. doi:10.1016/j.tibs.2010.06.003.

[3] D. Lingwood, K. Simons, Lipid rafts as a membrane-organizing principle, Science. 327 (2010) 46–50. doi:10.1126/science.1174621.

[4] H.T. McMahon, E. Boucrot, Membrane curvature at a glance, J Cell Sci. 128 (2015) 1065–1070. doi:10.1242/jcs.114454.

[5] S. McLaughlin, J. Wang, A. Gambhir, D. Murray, PIP(2) and proteins: interactions, organization, and information flow, Annu. Rev. Biophys. Biomol. Struct. 31 (2002) 151–175. doi:10.1146/annurev.biophys.31.082901.134259.

[6] S. Suetsugu, S. Kurisu, T. Takenawa, Dynamic Shaping of Cellular Membranes by Phospholipids and Membrane-Deforming Proteins, Physiol. Rev. 94 (2014) 1219–1248. doi:10.1152/physrev.00040.2013.

[7] P.P. Cheney, A.W. Weisgerber, A.M. Feuerbach, M.K. Knowles, Single Lipid Molecule Dynamics on Supported Lipid Bilayers with Membrane Curvature, Membranes. 7 (2017). doi:10.3390/membranes7010015.

[8] N.S. Hatzakis, V.K. Bhatia, J. Larsen, K.L. Madsen, P.-Y. Bolinger, A.H. Kunding, J. Castillo, U. Gether, P. Hedegård, D. Stamou, How curved membranes recruit amphipathic helices and protein anchoring motifs, Nat. Chem. Biol. 5 (2009) 835–841. doi:10.1038/nchembio.213.

[9] A.M. Kabbani, X. Woodward, C.V. Kelly, Revealing the Effects of Nanoscale Membrane Curvature on Lipid Mobility, Membranes. 7 (2017) 60. doi:10.3390/membranes7040060.

[10] I.R. Cooke, M. Deserno, Coupling between Lipid Shape and Membrane Curvature, Biophys. J. 91 (2006) 487–495. doi:10.1529/biophysj.105.078683.

[11] T. Baumgart, B.R. Capraro, C. Zhu, S.L. Das, Thermodynamics and Mechanics of Membrane Curvature Generation and Sensing by Proteins and Lipids, Annu. Rev. Phys. Chem. 62 (2011) 483–506. doi:10.1146/annurev.physchem.012809.103450.

[12] R. Parthasarathy, C. Yu, J.T. Groves, Curvature-modulated phase separation in lipid bilayer membranes, Langmuir ACS J. Surf. Colloids. 22 (2006) 5095–5099. doi:10.1021/la060390o.
[13] M.O. Ogunyankin, A. Torres, F. Yaghmaie, M.L. Longo, Lipid domain pixelation patterns imposed by e-beam fabricated substrates, Langmuir ACS J. Surf. Colloids. 28 (2012) 7107–7113. doi:10.1021/la3008415.
[14] J. C. Black, P. P. Cheney, T. Campbell, M. K. Knowles, Membrane curvature based lipid sorting using a nanoparticle patterned substrate, Soft Matter. 10 (2014) 2016–2023. doi:10.1039/C3SM52522H.
[15] A.M. Kabbani, C.V. Kelly, The Detection of Nanoscale Membrane Bending with Polarized Localization Microscopy, Biophys. J. 113 (2017) 1782–1794. doi:10.1016/j.bpj.2017.07.034.
[16] A.M. Kabbani, C.V. Kelly, Nanoscale Membrane Budding Induced by CTxB and Detected via Polarized Localization Microscopy, Biophys. J. 113 (2017) 1795–1806. doi:10.1016/j.bpj.2017.08.031.
[17] A. Callan-Jones, B. Sorre, P. Bassereau, Curvature-Driven Lipid Sorting in Biomembranes, Cold Spring Harb. Perspect. Biol. 3 (2011). doi:10.1101/cshperspect.a004648.
[18] M. Heinrich, A. Tian, C. Esposito, T. Baumgart, Dynamic sorting of lipids and proteins in membrane tubes with a moving phase boundary, Proc. Natl. Acad. Sci. 107 (2010) 7208–7213. doi:10.1073/pnas.0913997107.
[19] A. Roux, D. Cuvelier, P. Nassoy, J. Prost, P. Bassereau, B. Goud, Role of curvature and phase transition in lipid sorting and fission of membrane tubules, EMBO J. 24 (2005) 1537–1545. doi:10.1038/sj.emboj.7600631.
[20] B. Sorre, A. Callan-Jones, J.-B. Manneville, P. Nassoy, J.-F. Joanny, J. Prost, B. Goud, P. Bassereau, Curvature-driven lipid sorting needs proximity to a demixing point and is aided by proteins, Proc. Natl. Acad. Sci. U. S. A. 106 (2009) 5622–5626. doi:10.1073/pnas.0811243106.
[21] A. Tian, T. Baumgart, Sorting of Lipids and Proteins in Membrane Curvature Gradients, Biophys. J. 96 (2009) 2676–2688. doi:10.1016/j.bpj.2008.11.067.
[22] Y.A. Domanov, S. Aimon, G.E.S. Toombes, M. Renner, F. Quemeneur, A. Triller, M.S. Turner, P. Bassereau, Mobility in geometrically confined membranes, Proc. Natl. Acad. Sci. U. S. A. 108 (2011) 12605–12610. doi:10.1073/pnas.1102646108.
[23] S.L. Veatch, Electro-formation and fluorescence microscopy of giant vesicles with coexisting liquid phases, Methods Mol. Biol. Clifton NJ. 398 (2007) 59–72. doi:10.1007/978-1-59745-513-8_6.
[24] X. Shi, M. Kohram, X. Zhuang, A.W. Smith, Interactions and Translational Dynamics of Phosphatidylinositol Bisphosphate (PIP2) Lipids in Asymmetric Lipid Bilayers, Langmuir ACS J. Surf. Colloids. 32 (2016) 1732–1741. doi:10.1021/acs.langmuir.5b02814.
[25] M. Ovesný, P. Křížek, J. Borkovec, Z. Svindrych, G.M. Hagen, ThunderSTORM: a comprehensive ImageJ plug-in for PALM and STORM data analysis and super-resolution imaging, Bioinforma. Oxf. Engl. 30 (2014) 2389–2390. doi:10.1093/bioinformatics/btu202.
[26] J. Schindelin, I. Arganda-Carreras, E. Frise, V. Kaynig, M. Longair, T. Pietzsch, S. Preibisch, C. Rueden, S. Saalfeld, B. Schmid, J.-Y. Tinevez, D.J. White, V. Hartenstein, K. Eliceiri, P. Tomancak, A. Cardona, Fiji: an open-source platform for biological-image analysis, Nat. Methods. 9 (2012) 676–682. doi:10.1038/nmeth.2019.
[27] K. Jaqaman, D. Loerke, M. Mettlen, H. Kuwata, S. Grinstein, S.L. Schmid, G. Danuser, Robust single-particle tracking in live-cell time-lapse sequences, Nat. Methods. 5 (2008) 695–702. doi:10.1038/nmeth.1237.
[28] D. Oh, Y. Yu, H. Lee, B.L. Wanner, K. Ritchie, Dynamics of the Serine Chemoreceptor in the Escherichia coli Inner Membrane: A High-Speed Single-Molecule Tracking Study, Biophys. J. 106 (2014) 145–153. doi:10.1016/j.bpj.2013.09.059.

[29] S.M. Sterling, E.S. Allgeyer, J. Fick, I. Prudovsky, M.D. Mason, D.J. Neivandt, Phospholipid diffusion coefficients of cushioned model membranes determined via z-scan fluorescence correlation spectroscopy, Langmuir ACS J. Surf. Colloids. 29 (2013) 7966–7974. doi:10.1021/la400768s.
[30] N. Bag, D.H.X. Yap, T. Wohland, Temperature dependence of diffusion in model and live cell membranes characterized by imaging fluorescence correlation spectroscopy, Biochim. Biophys. Acta. 1838 (2014) 802–813. doi:10.1016/j.bbamem.2013.10.009.
[31] A.S. Reddy, D.T. Warshaviak, M. Chachisvilis, Effect of membrane tension on the physical properties of DOPC lipid bilayer membrane, Biochim. Biophys. Acta. 1818 (2012) 2271–2281. doi:10.1016/j.bbamem.2012.05.006.
[32] S. Ramadurai, R. Duurkens, V.V. Krasnikov, B. Poolman, Lateral Diffusion of Membrane Proteins: Consequences of Hydrophobic Mismatch and Lipid Composition, Biophys. J. 99 (2010) 1482–1489. doi:10.1016/j.bpj.2010.06.036.
[33] C. Zhu, S.L. Das, T. Baumgart, Nonlinear Sorting, Curvature Generation, and Crowding of Endophilin N-BAR on Tubular Membranes, Biophys. J. 102 (2012) 1837–1845. doi:10.1016/j.bpj.2012.03.039.
[34] A.M.T.M. do Canto, J.R. Robalo, P.D. Santos, A.J.P. Carvalho, J.P.P. Ramalho, L.M.S. Loura, Diphenylhexatriene membrane probes DPH and TMA-DPH: A comparative molecular dynamics simulation study, Biochim. Biophys. Acta. 1858 (2016) 2647–2661. doi:10.1016/j.bbamem.2016.07.013.
[35] M.J. Skaug, M.L. Longo, R. Faller, The impact of Texas red on lipid bilayer properties, J. Phys. Chem. B. 115 (2011) 8500–8505. doi:10.1021/jp203738m.
[36] M.J. Skaug, M.L. Longo, R. Faller, Computational studies of Texas Red-1,2-dihexadecanoyl-sn-glycero-3-phosphoethanolamine-model building and applications, J. Phys. Chem. B. 113 (2009) 8758–8766. doi:10.1021/jp902877y.
[37] K. Kachel, E. Asuncion-Punzalan, E. London, The location of fluorescence probes with charged groups in model membranes, Biochim. Biophys. Acta. 1374 (1998) 63–76. doi:10.1016/S0005-2736(98)00126-6.
[38] K.J. Seu, A.P. Pandey, F. Haque, E.A. Proctor, A.E. Ribbe, J.S. Hovis, Effect of Surface Treatment on Diffusion and Domain Formation in Supported Lipid Bilayers, Biophys. J. 92 (2007) 2445–2450. doi:10.1529/biophysj.106.099721.
[39] C. Scomparin, S. Lecuyer, M. Ferreira, T. Charitat, B. Tinland, Diffusion in supported lipid bilayers: Influence of substrate and preparation technique on the internal dynamics, Eur. Phys. J. E. 28 (2009) 211–220. doi:10.1140/epje/i2008-10407-3.
[40] R. Macháň, M. Hof, Lipid diffusion in planar membranes investigated by fluorescence correlation spectroscopy, Biochim. Biophys. Acta BBA - Biomembr. 1798 (2010) 1377–1391. doi:10.1016/j.bbamem.2010.02.014.
[41] Y. Okamoto, T. Motegi, K. Morita, T. Takagi, H. Amii, T. Kanamori, M. Sonoyama, R. Tero, Lateral Diffusion and Molecular Interaction in a Bilayer Membrane Consisting of Partially Fluorinated Phospholipids, Langmuir. 32 (2016) 10712–10718. doi:10.1021/acs.langmuir.6b02874.
[42] L. Zhang, S. Granick, Lipid diffusion compared in outer and inner leaflets of planar supported bilayers, J. Chem. Phys. 123 (2005) 211104. doi:10.1063/1.2138699.
[43] I. Urbančič, A. Ljubetič, Z. Arsov, J. Štrancar, Coexistence of Probe Conformations in Lipid Phases—A Polarized Fluorescence Microspectroscopy Study, Biophys. J. 105 (2013) 919–927. doi:10.1016/j.bpj.2013.07.005.
[44] S.E. Sund, J.A. Swanson, D. Axelrod, Cell membrane orientation visualized by polarized total internal reflection fluorescence., Biophys. J. 77 (1999) 2266–2283. doi:10.1016/S0006-3495(99)77066-9.

[45] H. Raghuraman, S. Shrivastava, A. Chattopadhyay, Monitoring the looping up of acyl chain labeled NBD lipids in membranes as a function of membrane phase state, Biochim. Biophys. Acta. 1768 (2007) 1258–1267. doi:10.1016/j.bbamem.2007.02.001.
[46] B. Nuscher, F. Kamp, T. Mehnert, S. Odoy, C. Haass, P.J. Kahle, K. Beyer, Alpha-synuclein has a high affinity for packing defects in a bilayer membrane: a thermodynamics study, J. Biol. Chem. 279 (2004) 21966–21975. doi:10.1074/jbc.M401076200.
[47] E. Gielen, N. Smisdom, M. vandeVen, B. De Clercq, E. Gratton, M. Digman, J.-M. Rigo, J. Hofkens, Y. Engelborghs, M. Ameloot, Measuring diffusion of lipid-like probes in artificial and natural membranes by raster image correlation spectroscopy (RICS): use of a commercial laser-scanning microscope with analog detection, Langmuir ACS J. Surf. Colloids. 25 (2009) 5209–5218. doi:10.1021/la8040538.
[48] H. Bouvrais, T. Pott, L.A. Bagatolli, J.H. Ipsen, P. Méléard, Impact of membrane-anchored fluorescent probes on the mechanical properties of lipid bilayers, Biochim. Biophys. Acta. 1798 (2010) 1333–1337. doi:10.1016/j.bbamem.2010.03.026.